THE ASTROPHYSICAL JOURNAL, 464:272–285, 1996 June 10

AN INFRARED STUDY OF THE VELOCITY STRUCTURE OF THE COMETARY COMPACT H II REGION G29.96−0.02

STUART L. LUMSDEN
Anglo-Australian Observatory, P.O. Box 296, Epping NSW 2121, Australia
AND
MELVIN G. HOARE
Max-Planck-Institut für Astronomie, Königstuhl 17, D-69117, Heidelberg, Germany
Received 1995 July 17; accepted 1996 January 5

ABSTRACT

We have mapped the velocity structure of the cometary compact H II region G29.96−0.02 using long-slit echelle spectra of the Brγ line. This technique detects line emission over a much wider area at the necessary spatial resolution compared to radio recombination line observations. Significant structure in both the velocity centroids and the line widths is seen over the entire nebula. Large line widths are seen ahead of the bow and in the tail, which may be due to turbulent motions in shocked and interface regions, respectively. We construct analytic models of the density and velocity structure in order to attempt to distinguish between the bow shock and champagne flow models that have been put forward to explain the cometary morphology of many compact H II regions. The bow shock model is unable to explain the large velocity gradient that we see right across the tail of the cometary region, which can be explained only by the streaming motions toward low-density regions in the champagne model. However, our approximation to the champagne model is also not able to fit all of the features of the data. More realistic versions of this model that include the effects of stellar winds and density gradients may be able to provide a better match to these data.

Subject headings: H II regions — ISM: individual (G29.96−0.02) — ISM: kinematics and dynamics — shock waves

1. INTRODUCTION

Young hot stars have a dramatic effect on their surroundings when they first begin to ionize the ambient molecular gas to form H II regions. These effects are perhaps most important in their relation to further star formation; do they trigger further collapse through compression (Elmegreen & Lada 1977) or ultimately halt the process because of dispersal of the molecular cloud (see, e.g., Franco, Shore, & Tenorio-Tagle 1994)? The most compact and heavily embedded sources have attracted particular attention since they have been presumed to be the youngest and therefore most relevant to high-mass star formation. These small, dense regions are easily visible across great distances at radio wavelengths via their free-free emission and at far-infrared wavelengths since the hot stars also heat the associated dust.

The study of ultracompact (UC) H II regions in particular has been stimulated in recent years by the sparsely sampled VLA survey of Wood & Churchwell (1989). One of the greatest puzzles of the Wood & Churchwell survey is the total number of such regions found. By taking both the total number of O stars in the galaxy (simply from extrapolating the number of optically visible OB associations), and their lifetimes on the main sequence, they predicted the total number of such sources that might still be expected to be in the UC H II phase. Comparing this with the numbers actually found led Wood & Churchwell to conclude that there was an order of magnitude more sources in their VLA survey than there should have been. Since there is no other evidence for the massive star formation rate being this much larger than expected, the likeliest solution to this problem is that some mechanism is constraining the outward expansion of the H II region. Wood & Churchwell estimate that the UC H II phase must last about 10 times longer than the $\sim 10^4$ yr predicted on the basis of simple Strömgren sphere expansion.

Another key result from the Wood & Churchwell study is that about 20% of these regions have a "cometary" appearance. A subsequent survey by Kurtz, Churchwell, & Wood (1994) and a VLA survey of much larger, optically visible, H II regions by Fich (1993) also found a similar proportion of this type. The near-parabolic shape of many of these sources led Wood & Churchwell to develop a bow shock interpretation for UC H II regions that provides an explanation for both of the lifetime of the UC H II region phase and the cometary morphologies. The basis of this model is simple. An OB star moves supersonically through a molecular cloud ($v_* > 0.2$ km s^{-1}), and the stellar wind from the star supports a bow shock along its direction of motion. This shock can trap the ionization front (IF), preventing it from expanding. Such a situation is potentially stable, and the lifetime of the UC H II phase in this model is simply the star's crossing time through the cloud, typically of the order of 10^5 yr.

Cometary-like morphologies for H II regions have been known for some time and were originally labeled "blisters" by Israel (1978) because of their propensity for being found near the edges of molecular clouds. Icke, Gatley, & Israel (1980) developed the idea that if there is a density gradient in the ambient gas, the H II region will expand fastest in the low-density direction and so become very asymmetric. Tenorio-Tagle and co-workers in a series of papers (Tenorio-Tagle 1979; Bodenheimer, Tenorio-Tagle, & Yorke 1979; Tenorio-Tagle, Yorke, & Bodenheimer 1979; Yorke, Tenorio-Tagle, & Bodenheimer 1983, 1984) examined the gasdynamics of this situation and found that the

pressure gradient set up when the IF reaches the edge of the cloud causes a "champagne" flow of ionized gas away from the cloud with velocities of order 30 km s^{-1}. They also give predictions for line profiles and for the expected radio continuum. This model does not answer the lifetime problem, however, since there is no constraint on the H II region expansion. Crucially, it also does not include the effects of the stellar wind from the OB star. Turner & Matthews (1984) considered the latter problem in a uniform static configuration: they find the IF could be trapped at early times in the shell formed by the stellar wind sweeping up the dense ambient gas ($n_e \sim 10^5$ cm^{-3}). A combination of this effect and the blister geometry plausibly satisfies both the lifetime and morphology constraints. The combined model would have a shell structure near the core and diffuse emission near the tail where lower densities preclude the trapping of the IF.

The bow shock and champagne models for cometary H II regions can be distinguished by the velocity structure of the ionized gas. Several studies have been carried out using radio recombination lines to map out the velocity structure. Garay, Rodríguez, & van Gorkom (1986) concluded that the cometary region in the G34.3+0.2 complex exhibits a champagne flow but also shows a large velocity gradient perpendicular to the symmetry axis, which they attributed to rotation of the parent cloud. A lower resolution study of the same object by Gaume, Fey, & Claussen (1994) found a similar velocity structure, but they reject both bow shock and champagne flow models in preference to a picture involving interactions with outflows from other sources ahead of the bow. Similar velocity structures have been seen in two cometary regions in the Sgr B2 complex by Gaume & Claussen (1990). Garay, Lizano, & Gomez (1994) presented radio recombination line maps of more extended H II regions and find evidence for a bow shock in one and champagne flows in two other more clumpy sources. Wood & Churchwell (1991) carried out high-resolution radio recombination line studies of the cometary UC H II region G29.96−0.02. Their results were analyzed by Van Buren & Mac Low (1992), who claim good agreement with their bow shock model.

There are substantial problems with the radio recombination line approach. These lines are intrinsically very weak, and since they arise from levels well above the ground state (Wood & Churchwell 1991 used H76α), they are prone to many broadening effects and maser activity. The high spatial resolution interferometric observations detect only the lines near the head of the bow and resolve out the weaker and more diffuse tail emission. The synthesized beam sizes required to detect the radio recombination lines in the tail are usually then too large to resolve the head region simultaneously. By contrast, infrared recombination lines are intrinsically brighter, and the detector technology is such that we can map emission across much larger regions where the surface brightness of the line emission is lower at high and uniform spatial resolution. Even allowing for the large extinction in these objects ($A_V \sim 20$–30 is typical, and much larger values possible), mapping the H I Brγ or Brα emission provides many potential benefits over further radio surveys.

We have therefore embarked on a series of IR observations of UC H II regions selected from Wood & Churchwell (1989) and from Kurtz, Churchwell, & Wood (1994). In this paper we demonstrate the value of our method by presenting observations and analysis of the prototypical cometary UC H II region: G29.96−0.02. In future papers, we will present further observations.

2. OBSERVATIONS

We used a broadband K_n image obtained with the near-infrared camera/spectrometer IRIS on the AAT to determine slit positions on the target. These positions are shown in Figure 1, overlaid on a contour map of the K_n image. The image has been rotated by 120° east from north. The near-infrared morphology of G29.96−0.02 is similar to the radio data presented in, for example, Afflerbach et al. (1994) or Fey et al. (1995). We will refer to the "head" of the region as being that portion at the top of Figure 1, while the "tail" is the broad fan shape at the bottom. Also of note in the contour map is the bright star located 2″ behind the "head" of the H II region, which we identify as a possible candidate for the exciting star for the region. Other stars are also evident in the field of view, but these do not appear to have associated ionized gas. We also obtained "snapshot" images at J and H as well to determine the nature of this star.

The high-resolution spectra were obtained with the common user IR array spectrometer CGS4 (Mountain et al. 1990) on UKIRT on the night of 1994 June 23. We used the echelle grating within CGS4, with a 1 pixel wide slit (each pixel corresponded to 1.″1 in the dispersion direction and 2.″0 along the slit). The effective resolution of this combination was measured to be 21.2 km s^{-1} on a completely unresolved bright OH night-sky line. To fully sample the resolution element, the array was stepped 6 times across 2 pixels. This oversampling is extremely useful in determining accurate line profiles for our data. Our basic observing technique was to observe at each position for 10 minutes (composed of five 2 minute exposures) and then to take a separate 2 minute sky frame. The slit was set at a position angle of 120°, as shown by Figure 1, in order to be approximately along the axis of G29.96−0.02, and we stepped 2″ between each position (so that we are undersampled spatially).

The echelle in CGS4 uses a circular variable filter (CVF) as an order sorter. This CVF can introduce significant fringing into the final image. To compensate for this, we obtained "fringe frames," by observing the flat-field lamp in the same manner as we observed the objects. Since our object is extended like the lamp, dividing all frames by this pattern removed virtually all trace of the fringing.

The wavelength region observed contains only one bright sky line and a few much weaker ones. To remove the night-sky emission, we used the median of all the separate sky frames and subtracted this from each 2 minute object exposure. The 2 minute exposures for each position were then averaged. One of the features of the echelle optics used in CGS4 is that the projection of the slit onto the array is curved. We removed this curvature by obtaining distortion corrections based on the strong night-sky emission line at 2.17114 μm (Oliva & Origlia 1992; note: all wavelengths are quoted in vacuum) from our median sky frame.

To wavelength-calibrate our spectra we used an internal argon lamp within CGS4. There is a strong line at 2.167561 μm (Humphreys 1973) that was visible within our wavelength range. We assume a purely linear shift in the wavelength scale (which we have been assured is reliable for the echelle grating by the UKIRT staff). For the pixel with the

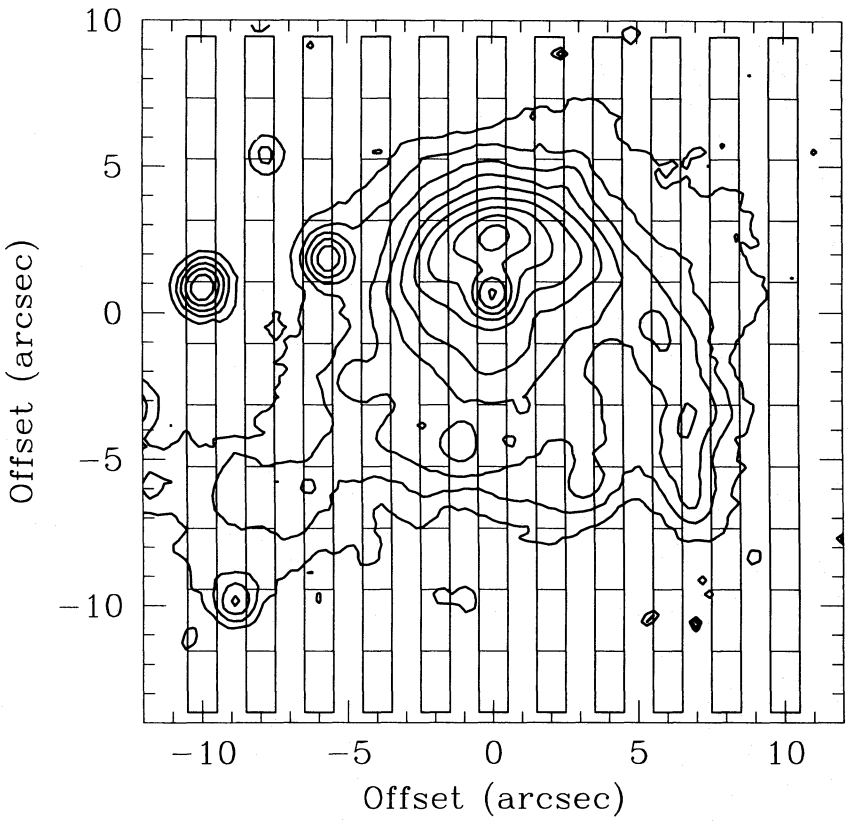

FIG. 1.—Position of the 11 slit positions used superimposed on a *K*-band contour map of G29.96−0.02. Contours are equally spaced logarithmically from 3% to 100% of peak flux.

largest flux [at offset (−2, +2.1)], we find $v_{\rm LSR} = 95 \pm 5$ km s^{-1}, where the error reflects uncertainties in the correction to LSR velocities, in our measured wavelengths and in the chosen rest wavelength for hydrogen (we assumed a wavelength of 2.166125 μm using the values for energy levels given in Bashkin & Stoner 1975). For the same position (that of peak radio flux), Wood & Churchwell (1991) quote a velocity of 98 km s^{-1} (no error is given), and Afflerbach et al. (1994) quote (92–96) ± 4 km s^{-1} for a similar position and beam size to ours. If we use the OH night-sky line to calibrate the data, we would have a velocity that was some 20 km s^{-1} too large. Therefore, we find that the value quoted for the wavelength of this line is inaccurate to this amount.

Observations were also made of BS 7377, a F3 IV star with $K = 2.52$, which served both as a flux and atmospheric standard. In practice, it proved impossible to remove all the CVF fringes from this object (probably because of the star's being effectively an unresolved source in the slit, whereas the flat-field correction is a diffuse illumination). We checked all our spectra to ensure that the line emission was in a region free of significant atmospheric absorption, rather than actually dividing by this standard. We used the relative counts in object and standard to flux calibrate our data. For the same pixel for which we compared the wavelength calibration, this results in a Brγ flux of 5.9×10^{-16} W m^{-2}. Our maps can be calibrated from this value using Figure 7. By fitting the weak Brγ absorption line in this standard and using the known radial velocity, we derived another check on the wavelength calibration. We found this calibration gave a wavelength for the pixel with the largest flux of 105 ± 10 km s^{-1}. This agreed with the calibration using the arc line (within the errors, which are mostly due to the CVF fringing). We are therefore confident of our wavelength calibration within the error quoted. We also used the standard star observations to monitor the seeing: we estimate that throughout these observations it was 1″–2″.

3. RESULTS

We obtained very short "snapshot" images (typically 10 s on object and 10 s on sky) in J, H, and K_n using IRIS to estimate the magnitude of the putative exciting star. From these, we find $K_n = 11.2$, $H = 12.8$, and $J = 15.2$ (with typical errors of ~0.3–0.5 mag due to [1] the short exposures and [2] the difficulty in separating the stellar component from the free-free background of the nebula). We can convert these into absolute magnitude given the extinction and the distance to the source. By comparing the observed Brγ flux in a large beam with the radio flux at a sufficiently high frequency that the radio continuum is optically thin we can estimate $\tau_{\rm Br\gamma}$ (cf. Lumsden & Puxley 1995). There are two published values for large-aperture Brγ fluxes: Doherty et al. (1994) found a flux of 2.5×10^{-15} W m^{-2} in a 5″ aperture centered on the continuum peak; Herter et al. (1981) found a flux of 7.6×10^{-15} W m^{-2} in a 12″ aperture; and, last, summing over our sparsely sampled emission-line map (Fig. 2), we find a flux of 7.3×10^{-15} W m^{-2} over the whole source. We believe the latter two values are more representative of the actual total flux in the H II region and use the Herter et al. value below since it does not suffer from the sparse sampling problems our CGS4 data does. There are two high-frequency radio measurements with suitable spatial resolution: Wood & Churchwell (1989) find that the 15 GHz integrated flux density is 2.661 Jy, and Cesaroni et al. (1994) find that the 24 GHz flux density is 3.534 Jy. We prefer to use the latter value since the VLA

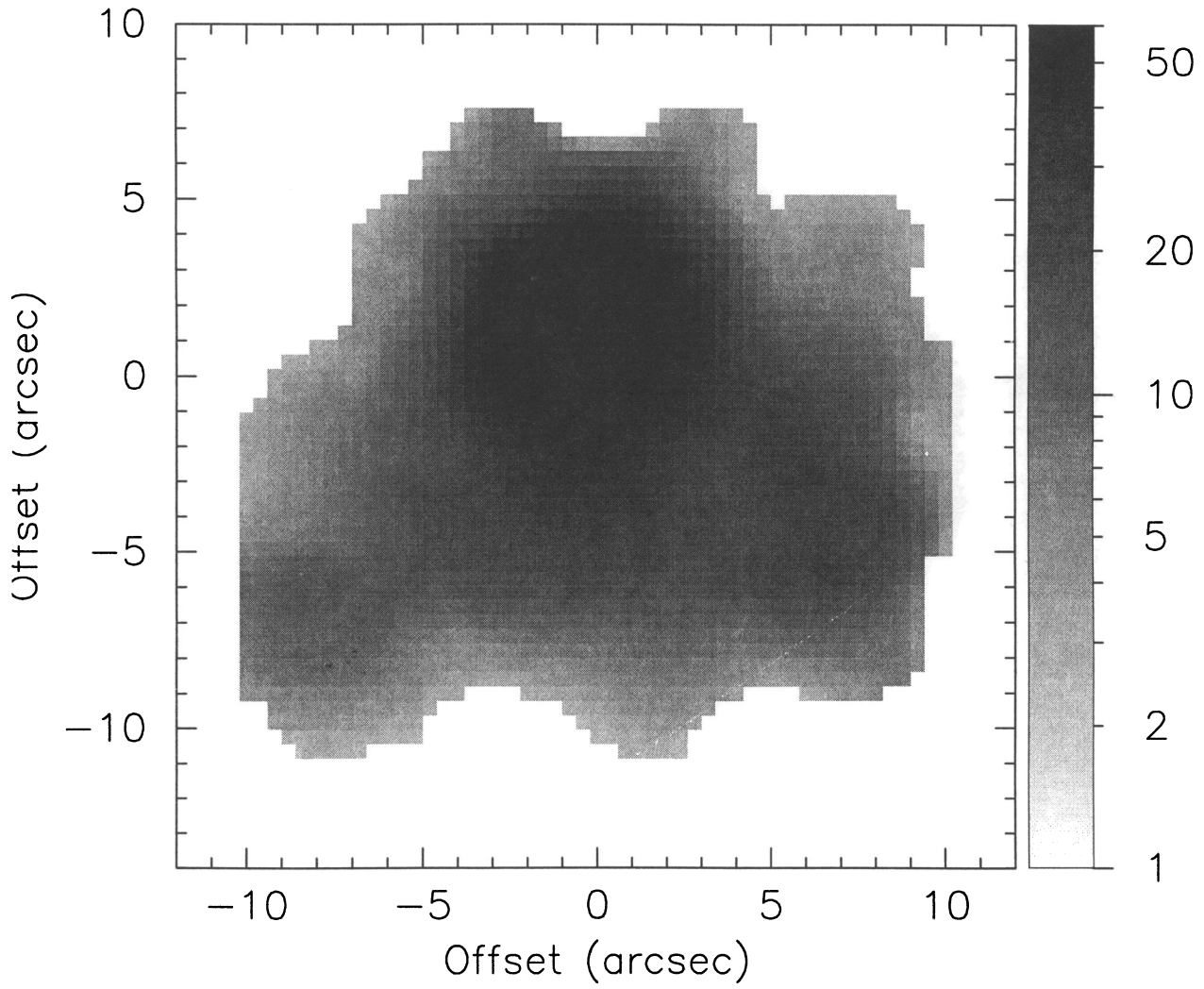

FIG. 2.—Gray-scale image of the line flux derived from our spectra, on the same scale as Fig. 1. The data are plotted logarithmically, and the scale given is log ($F_{Br\gamma}/5.5 \times 10^{-18}$ W m^{-2}). Sampling is effectively every 2″—the images are shown on a finer grid for display purposes only, as are those in Figs. 3 and 4. Only points with a signal-to-noise ratio in the integrated flux greater than 25 are shown. Note that we have recovered the same structure seen in the *K*-band image and low-resolution radio maps.

configuration used gave slightly greater sensitivity to the extended emission that is clearly missing from the Wood & Churchwell data (compare our K_n map with their 15 GHz one, for example) and also because the continuum opacity will be even less of a problem at 24 GHz. Assuming an electron temperature of 7500 K (which is consistent with the scatter in the values found by Afflerbach et al. 1994) and using the appropriate Brγ emissivity from Hummer & Storey (1987), this gives a total expected Brγ flux of 5×10^{-14} W m^{-2}. Hence, we find $\tau_{Br\gamma} = 1.9$. Using the extinction law of Landini et al. (1984), this corresponds to $A_K = 2.0$, $A_H = 3.4$, and $A_J = 5.7$ (and by further extrapolation $A_V = 24$). These values compare extremely well with those derived from a comparison of the observed and expected near-IR H I line strengths (T. Moore, private communication). For an assumed distance of 7.4 kpc (Churchwell, Walmsley, & Cesaroni 1990), we therefore derive absolute magnitudes for the star(s) of $M_K = -5.1$, $M_H = -4.9$, and $M_J = -4.8$. Comparison with the colors expected of main-sequence O stars (Koornneef 1983) shows reasonable agreement with the relative *JHK* values within the errors given above. From the expected optical-infrared colors, we derive $M_V \sim -6.0$, which is typical of an O3 V star. This value is consistent with that obtained from the radio and far-infrared data (Wood & Churchwell 1989 give the type as O4–O5, which have $M_V = -5.7 \rightarrow -5.9$). However, given the absence of strong 10.5 μm [S IV] emission in G29.96−0.02 (see, e.g., Herter et al. 1981), which we would expect to be present for a single star of this type, it is likely that the exciting source is in fact a cluster of stars. The hottest star is likely to be of type O6 at most with this constraint (see also the arguments presented about the very similar compact H II region, G45.12+0.13, in Lumsden & Puxley 1995).

All our CGS4 spectra were fitted by a single Gaussian line profile using the Starlink DIPSO package. We allowed the intensity, central wavelength, and line width to vary. A Gaussian is a good match to the instrumental line profile (found by fitting the night-sky emission line). Except where the signal-to-noise ratio was very low, we found that a Gaussian was generally a good match to the observed Brγ profile. There is some small amount of evidence for weak line splitting near the head and the tail (see also § 4.1). There was negligible continuum emission in our position.

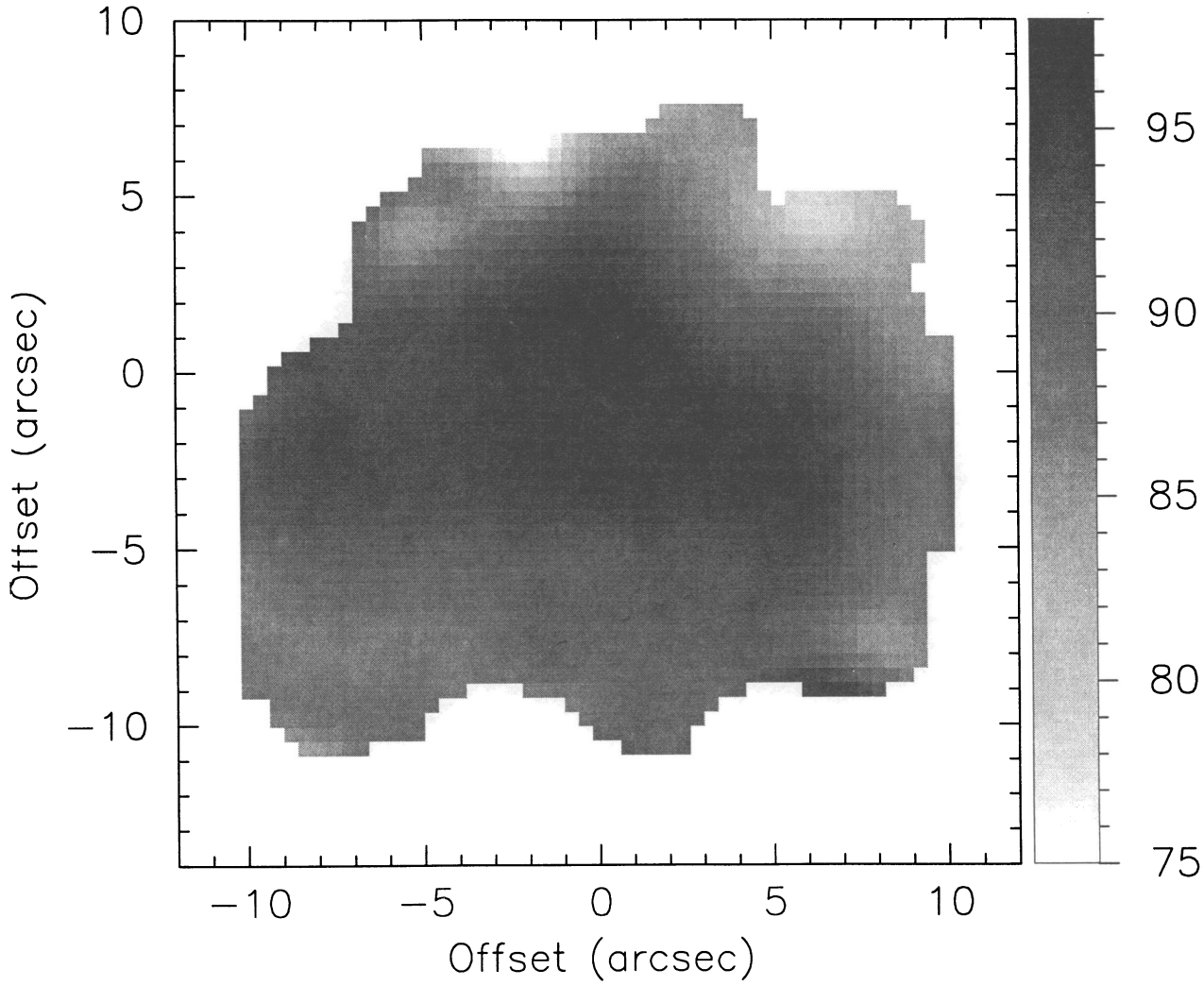

FIG. 3.—Gray-scale image of the velocity centroid derived from Gaussian fits to our spectra. Contour levels are equally spaced from v_{LSR} = 75 km s^{-1} (*white*) to 98 km s^{-1} (*black*). The contours are perpendicular to the cometary axis in the tail indicating streaming motion out of the tail.

We present the results of our Gaussian fits to the observations in image form in Figures 2, 3, and 4, where we have excluded those points with the lowest signal-to-noise ratio (by trial and error, a signal-to-noise ratio of ~20 in the measured flux appears to be the minimum value for which the Gaussian line fitting parameters are entirely reliable). The flux map is very similar to the K_n-band continuum contour map shown in Figure 1. This is not surprising since in general the continuum emission at the short end of the K window is dominated by free-free processes and hence line and continuum should track each other.

We can also compare our data to those presented by Wood & Churchwell (1991) and Afflerbach et al. (1994). The former have the advantage of good spatial resolution but poorer sensitivity, while the latter have a larger beam but are more sensitive. The Wood & Churchwell map of the line emission covers an area of about 7″ × 6″; the Afflerbach map extends ~14″ along the tail but at much poorer spatial resolution (they had to use a 4.″2 beam to sample the gas in the tail and had to clearly smooth over much of the structure present as they note themselves). By contrast, our data accurately map the line emission across ~20″ × 17″ as shown in Figure 2. Our data are similar to the total extent and structure of the radio continuum emission in the Fey et al. (1995) or Cesaroni et al. (1994) continuum maps. We are therefore in a better position to probe the velocity structure in the important regions near the tail and around the edges of the cometary profile. As shown below, these provide important constraints on the models. Allowing for the different beam sizes involved, we find excellent agreement between our data and the data of both Wood & Churchwell and Afflerbach et al. where we overlap. The most obvious discrepancies between our data and the Wood & Churchwell data (which has received extensive attention) are (1) the line center velocity reaches a maximum near the line intensity peak and then turns over, such that the velocities seen near the tail are very similar to those at the head; and (2) the line widths are broader in all directions away from the intensity peak and not just toward the head. As we show below, taking account of these features leads us to rather different conclusions from those of Van Buren & Mac Low (1992).

4. MODELING

We have interpreted our velocity data by constructing an empirical model in which the three-dimensional density distribution and velocity structure are specified and the resultant simulated spectra are then compared to the observed quantities. This approach gives us flexibility and means we are not restricted to one particular model.

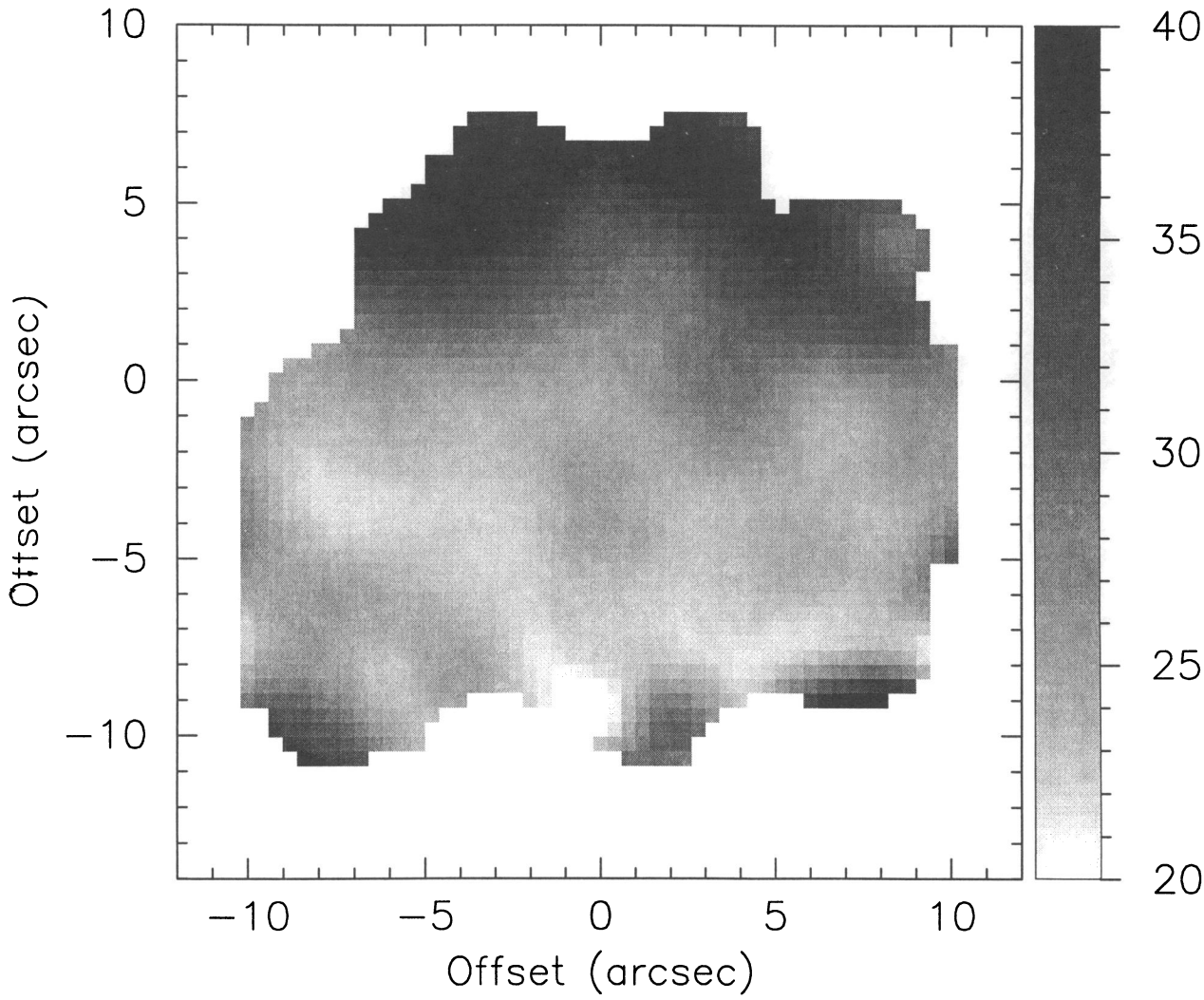

FIG. 4.—Gray-scale image of the line width derived from Gaussian fits to our spectra. Contour levels are equally spaced from 20 km s^{-1} (*white*) to 40 km s^{-1} (*black*). Note the large line widths ahead of the bow.

Our methodology resembles in some respects that used by Mac Low et al. (1991). In particular we follow the geometric layout of their Figure 11 in which our object is specified in a Cartesian system ($x'y'z'$) and is axisymmetric about the z' axis. The object frame is at an angle i relative to the observer's frame (xyz) rotated about the x' axis (parallel to the x-axis) and the observer is at $z = +\infty$. This geometry is illustrated in Figure 5.

We investigated the bow shock model first as this is more amenable to analytic specification. We attempted to use analytic forms to match closely the numerical models of Mac Low et al. (1991) that have already been compared to the radio recombination line data for G29.96−0.02 by Van Buren & Mac Low (1992). The shape of the bow shock was assumed to be described by the function

$$z' = r/\tan(r/l) \quad (1)$$

in cylindrical coordinates, where r is the radial coordinate parallel to the y'-axis. This shape was derived by Dyson (1975) and was shown to be a good approximation to the numerical solution calculated by Mac Low et al. with the tangent function slightly underestimating the divergence in the tail of the bow. The function intersects the z'-axis at $z' = l$, which was termed the standoff distance by Mac Low et al. The electron density distribution as a function of ϕ—the angle with respect to the z'-axis from the origin—was described by a Gaussian such that

$$n_e = n_e(\phi_0) \exp(-\phi^2/2\sigma_{n\phi}^2), \quad (2)$$

where $n_e(\phi_0)$ is the density on the z'-axis. A value of $\sigma_{n\phi} = 1$ closely approximates the distribution shown by Dyson (1975) in his Figure 5. To describe the thickness of the shell, we again use a Gaussian such that

$$n_e(\phi_0) = n_e(\max) \exp[-(l - l_{\max})^2/2\sigma_{nl}^2], \quad (3)$$

where $l_{\max}$ is the point on the z'-axis where the density is at a maximum. Regions where the density fell to less than 0.1% of the peak were not considered in the calculation.

The velocity distribution was specified so as to match the form given by the numerical models of Mac Low et al. illustrated in their Figure 3*a*. We assumed that the velocity is perpendicular to the shell (the velocity is defined relative to the ambient ISM in this case) since that seems to be the case to within about 10°. The falloff of speed with ϕ was assumed to be of the form

$$v_{\text{bow}} = v_*[1 - (\phi/c_\phi)^2]. \quad (4)$$

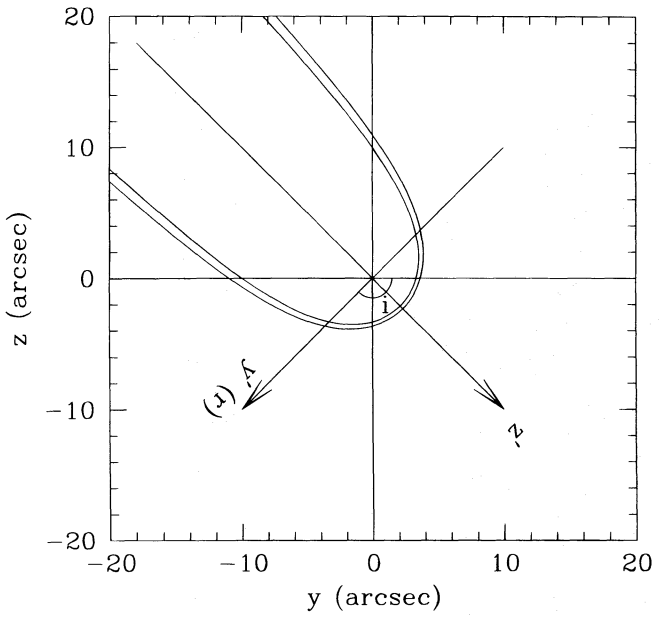

FIG. 5.—Geometry used in the models showing the definition of the object with the observer (xyz) frame and object ($x'y'z'$, rz') frame. The curve traces the FWHM of the density distribution for the model parameters in Table 1.

With $c_\phi = 3.0$ this closely approximates the numerical solution of Mac Low et al. v_* is the velocity of the star relative to the ambient cloud in the bow shock model. The density and velocity distributions are rotated about the z'-axis in order to give the three-dimensional structure.

The model was calculated on a Cartesian cube in the observer's frame of 101 points on each side with a step size of 0.″4 so that the total size of the cube is $\pm 20''$ from the origin. This was sufficient to sample the slit width and cover the entire area where emission was detected. We proceeded through each x, y point in the sky frame in turn and integrated along the z-axis to give the emission measure (EM) at each velocity such that

$$\mathrm{EM}(x, y, v) = \int n_e^2(x, y, z, v) dz \, . \tag{5}$$

To obtain the density and line-of-sight velocity at any one point, we first transformed the coordinates into the object frame (i.e., $x'y'z'$) . The equivalent cylindrical coordinate, r, is given by $(x'^2 + y'^2)^{1/2}$, and then l can be found from inverting equation 1. With ϕ given by arctan (r/z'), we obtained the density and velocity components in the object frame. The velocity components are transformed back into the observer's frame to give the z component of velocity for that point.

For the intrinsic spectrum of the Brγ line, we considered only thermal and turbulent broadening and assumed a Gaussian profile given by

$$\phi_D(v) = \frac{1}{(2\pi)^{1/2}\sigma_v} \exp\left[-\frac{(v - v_z)^2}{2\sigma_v^2}\right], \tag{6}$$

where

$$\sigma_v^2 = \frac{1}{2}\left(\frac{2kT}{m_\mathrm{H}} + v_\mathrm{turb}^2\right). \tag{7}$$

We assumed a constant electron temperature throughout the nebula of 6500 K as deduced from the radio recombination line observations of Afflerbach et al. (1994). The turbulent velocity was left as a free parameter to match the observed width of the lines and was also assumed to be constant over the nebula. Fifty frequency points covering ± 70 km s^{-1} were used.

For each frequency the emergent emission measure was then convolved with a Gaussian seeing profile of FWHM = 1.″0 and then integrated over the area of each pixel of each of the observed slit positions. The resultant spectrum was then convolved in the spectral direction with a Gaussian to represent the spectral resolution of the CGS4 spectrometer. In order to compare with the data, the synthesized spectra were subjected to the same Gaussian fitting process. The model parameters were varied until as reasonable a match as possible was obtained.

4.1. *Bow Shock Models*

The results for our best bow shock model as described above are shown in Figures 6 and 7 with the model parameters given in Table 1. Figure 6 shows the comparison of the flux, velocity centroid, and velocity width of the Gaussian fits to the model compared to those for the data along the direction of the slits, while Figure 7 shows the data from the same spectral row of each slit position, i.e., the data perpendicular to the slit direction. All the fluxes, both observed and model, have been normalized to the peak observed flux in the central slit position. In order to compare the synthesized velocity centroids with the data, we have subtracted a velocity offset which is another free parameter and is basically the v_LSR of the ambient cloud in the context of the bow shock model.

The two curves in Figure 5 trace the points at which the density has fallen to half its peak value, and the total integrated emission measure from this model is similar to that presented by Mac Low et al. (1991) for this source. As in the model by Van Buren & Mac Low, the best-fitting inclination angle appears to be $-135°$ (the head of the bow pointing away from us), and a stellar velocity of 20 km s^{-1} appears most appropriate. Our value of the standoff distance l_max, which is constrained by the need to fit the opening angle of the structure with equation (1), is over twice the 1.″3 derived by those authors. This is in the sense expected since the tangent function we use to describe the shape of the bow shock (eq. [1]) underestimates the divergence of the tail. It can be seen from the fit to the cross sections in the tail in Figure 7 that our analytic description still underestimates the width of the tail somewhat. Increasing l_max further does not improve the overall fit since this

TABLE 1

PARAMETERS FOR THE BOW SHOCK MODEL

Parameter	Value
Inclination i	$-135°$
Standoff distance l_max	3.″0
Angular density parameter $\sigma_{n\phi}$	1.2 rad
Shell thickness parameter σ_{nl}	0.″25
Angular velocity parameter c_ϕ	3.0 rad
Stellar velocity v_*	20 km s^{-1}
Turbulent velocity v_turb	10 km s^{-1}
Velocity offset with respect to V_LSR	82 km s^{-1}

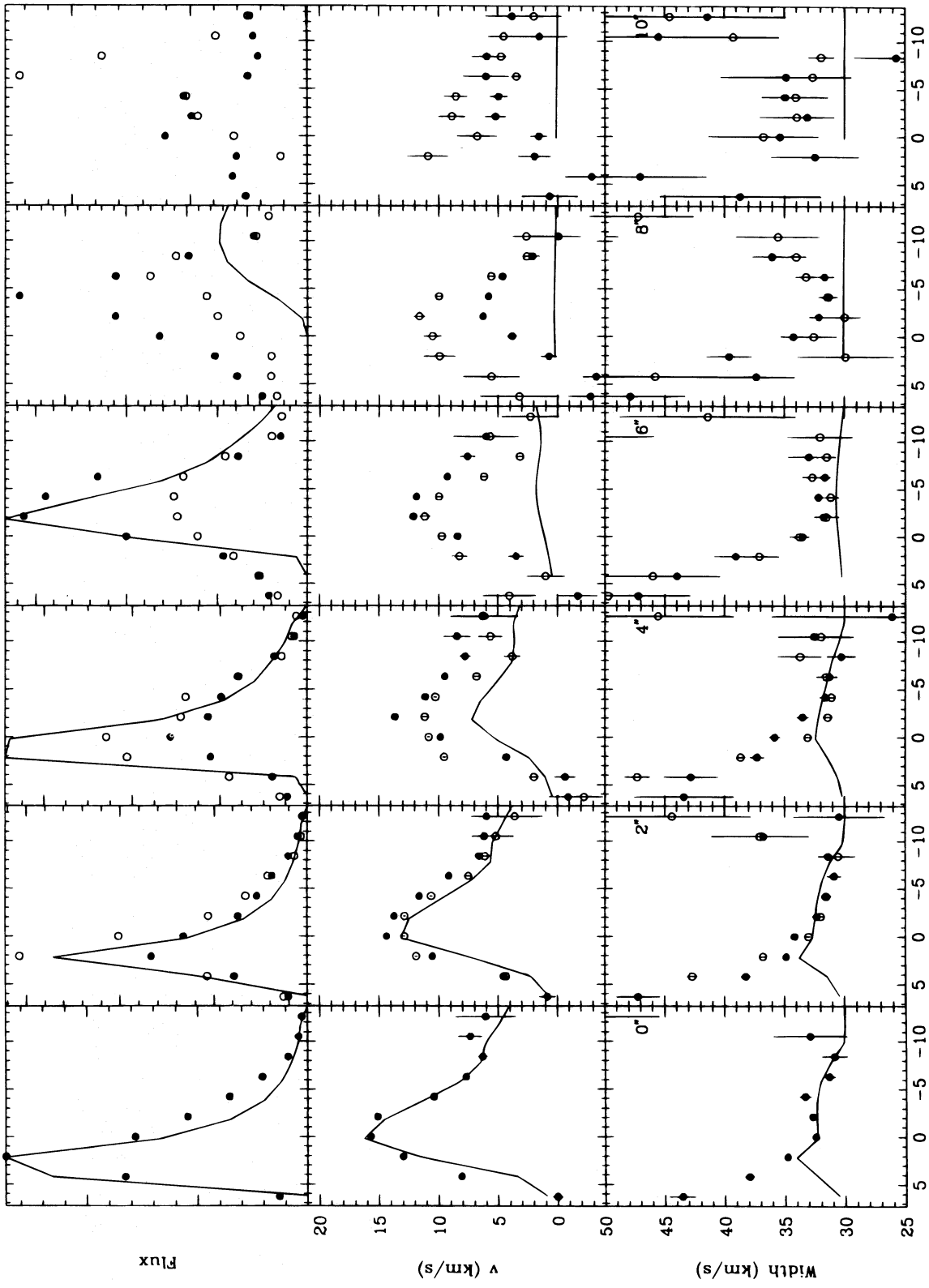

FIG. 6.—Flux, velocity centroid, and width of the bow shock model compared with the observational points along the slit. Each set of three vertical panels (except the first one which shows the on-axis data) shows the comparison for the two slit positions on opposite sides of the cometary axis with filled points for the positive offsets and open for the negative ones. The offset of the slit from the axis is shown in the top right-hand corner of the bottom panels. Note the lack of velocity gradient in the model compared to the observations in the slit positions which are a long way from the axis (*right-hand middle panels*).

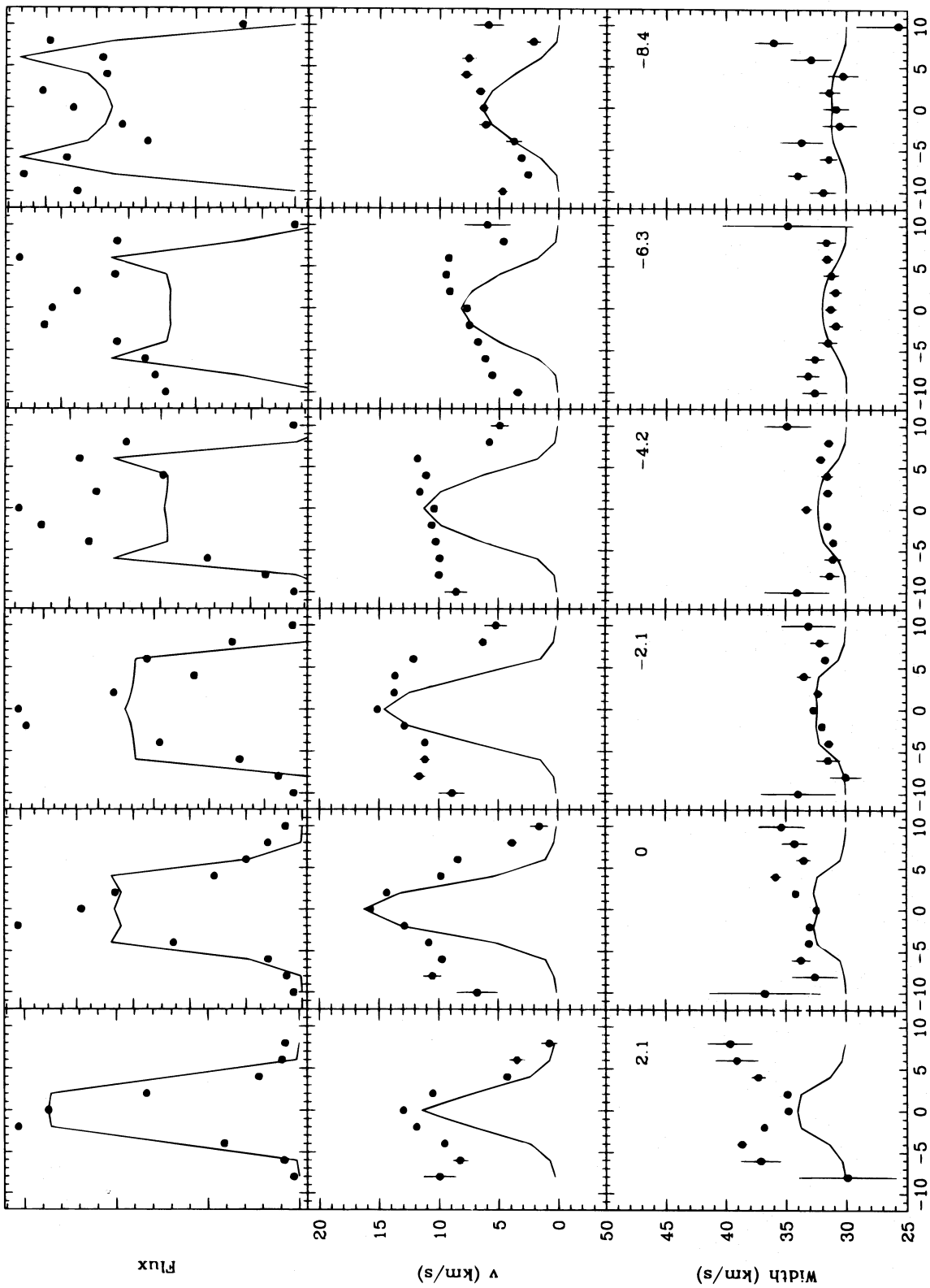

FIG. 7.—Flux, velocity centroid, and width of the bow shock model compared with the observational points perpendicular to the slit direction. Each set of three vertical panels shows the comparison for one cut perpendicular to the cometary axis. The offsets of the cuts are shown in the top right-hand corner of the bottom panels and go from cuts across the head on the left to cuts across the tail on the right. Note the velocity centroid distribution of the model is too narrow compared to the observations.

begins to displace the peak in the velocity centroid too far away from the flux peak. Obviously the tangent function is not a perfect description of the shape of G29.96−0.02.

As an aside, it is worth noting the position of the bright star (or cluster of stars) discussed in § 2. The projected standoff distance is 2".0, which for an inclination close to −135° (45°) is close to the deprojected value in the bow shock picture (see Fig. 5 of Mac Low et al. 1991). If this were the exciting star, as argued in § 3, then the inclination angle would have to be closer to −150° (30°) in order to agree with the standoff distance derived by Van Buren & Mac Low (1992). However, their estimate is strongly dependent on the stellar parameters used (e.g., stellar wind terminal velocity and mass-loss rate), and small changes to these mean that the observed position of the star is still compatible with their model.

The thickness of the shell (σ_{ne}) was set by matching the width of the peak in the flux distribution in the central slit position (the top left-hand panel of Fig. 6). This is only marginally resolved at our spatial resolution, so we also used the FWHM of the cuts through the radio continuum emission (see Wood & Churchwell 1989, Figs. 13 and 14) as a constraint. The chosen inclination angle and the angular density parameter ($\sigma_{n\phi}$) also significantly affect the width of the flux peak as well as the overall shape of the flux distribution along the central slit position. There is a certain lack of uniqueness among these parameters, and the inclination is determined to no better than about ±15°. However, these parameters do not greatly influence the pattern of the predicted velocity parameters which is of greater importance here.

It can be seen from the first two columns of Figure 6 that the bow shock model is a very good fit to the velocity centroid pattern near the head of the bow. The model is also a reasonable fit to the line widths in the region from the peak of the line emission toward the tail. A turbulent velocity of 8.5 km s^{-1} was found necessary to explain the minimum width we see in the data of about 30 km s^{-1} or 22 km s^{-1} deconvolved. However, the model is completely unable to explain the very steep increase in the line widths ahead of the emission peak. Here the lines of sight are tangential to the shell, and because of the required orientation, all the velocities are parallel to each other, and hence the lines should be relatively narrow. In the bow shock model, the highest intrinsic line widths arise near the stagnation point of the flow ahead of the bow, where the gas is streaming in all directions away from that point, but for the orientation of G29.96−0.02, the projected line width from this effect is small.

From the IR data alone, it might be supposed that these apparently high line widths are due to the observed spectrum being dominated by light scattered off dust in a dense shell of neutral material ahead of the bow. This would perhaps also explain the excess line flux observed ahead of the bow compared to the model that can be seen in the top row of Figure 6 as well as in the K_n band image in Figure 1. However, the radio recombination line data of Wood & Churchwell (1991) show exactly the same pattern of steeply increasing line widths *ahead* of the peak emission from the bow (see their Fig. 3). Since the radio data cannot be affected by scattered light, this is a real feature of the direct emission, and an alternative explanation must be found. Perhaps the most likely is that there is a partially ionized, highly turbulent layer ahead of the main bow shock itself. Indeed, in both the bow shock and champagne models, there is predicted to be a shock front ahead of the ionization front which could increase the turbulent velocity in this region.

Another notable difference between the model and the data lies in the increase in the line widths nearer the tail toward the edges of the nebula. This may be due to simple fluid instabilities in largely turbulent ionized gas (the passing star in the bow shock model largely evacuates the H II region, and therefore those regions well back in the "tail" will slowly fill in as the ionized and neutral gas at the molecular cloud interface merges). However, the current model as it stands is unable to explain this difference.

Further major deficiencies of the bow shock model can be seen in the regions away from the head. As the slit position is displaced further from the axis in Figure 6, the predicted velocity centroid becomes almost zero along the whole length of the object, whereas the observed points have a similar pattern to the central slit positions. Obviously in this model, most of the motion is directed radially outward in the tail, and so for slits close to the edge this is predominately tangential to the line of sight. A further illustration of this is seen in the velocity centroid cross sections in the tail in Figure 7. The observed velocity centroids stay redshifted right across the object until finally dropping toward the rest velocity outside of the well-defined rim at the edge in the south. The bow shock model necessarily has to follow the cosine-like falloff toward the edge. Some of this disagreement may be due to the fact that our assumed geometry is not a perfect match to that observed, but we believe that this is a major shortcoming of the bow shock model.

It is also difficult to reconcile the observed difference between the molecular and ionized gas velocities. Our velocity offset parameter of 82 km s^{-1}, which represents the LSR velocity of ambient molecular cloud, is much less than the value of ∼98 km s^{-1} given by Cesaroni et al. (1991) for various species. Another way to see this is that the peak velocity in the ionized gas, 100 ± 5 km s^{-1} from this work and 105 km s^{-1} from Wood & Churchwell (1991), is less than 10 km s^{-1} higher than the molecular gas, whereas the orientation and stellar velocity required in the bow shock model predict about 15 km s^{-1}.

In addition to comparing the data and models through Gaussian fits, we have also inspected the data and models for deviations from this line shape. In the observed line profiles, there is evidence of a slight excess on the red wing right across the brighter areas of the tail. Non-Gaussian profiles are also seen in the model in this region (where lines of sight cut through both the advancing and receding faces in the tail), however in the opposite sense, such that there is an excess on the blue wing and a deficit on the red.

4.2. *Champagne Models*

The presence of a velocity gradient along the edge of the cometary structure implies that the motion cannot be primarily radial but that there is a component parallel to the object axis as well. This is the main feature of the champagne model where ionized gas flows toward the low-density direction. There are only a few models currently in the literature that treat the more realistic case of an H II region expanding into a power law or exponential density gradient (see, e.g., Franco, Tenorio-Tagle, & Bodenheimer 1989). We have attempted only a very simplified prescription that incorporates the most basic features of the cham-

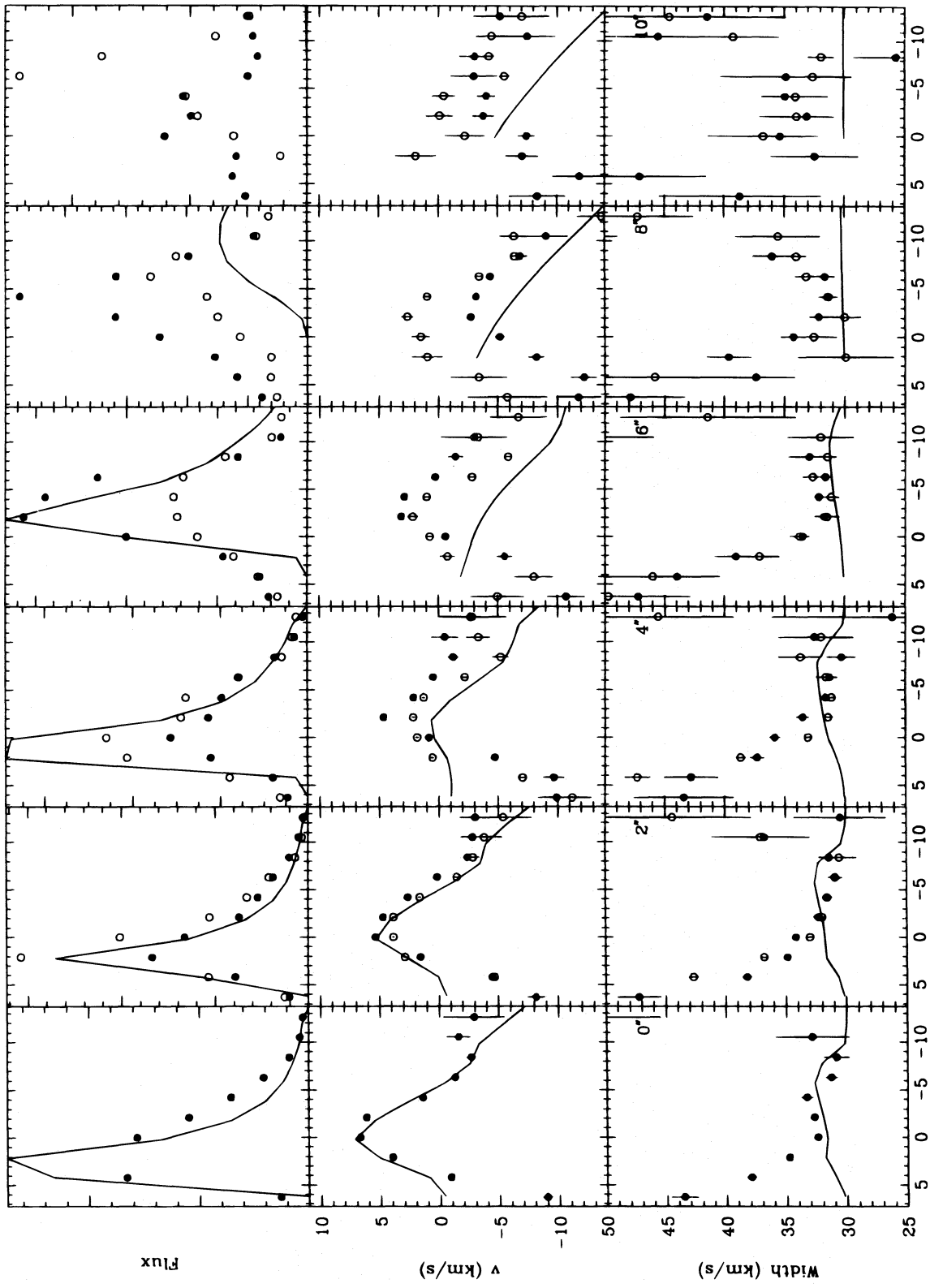

FIG. 8.—As in Fig. 7, but for the champagne model. Note the model also now has strong velocity gradients in the tail at large slit offset positions (*right-hand middle panels*).

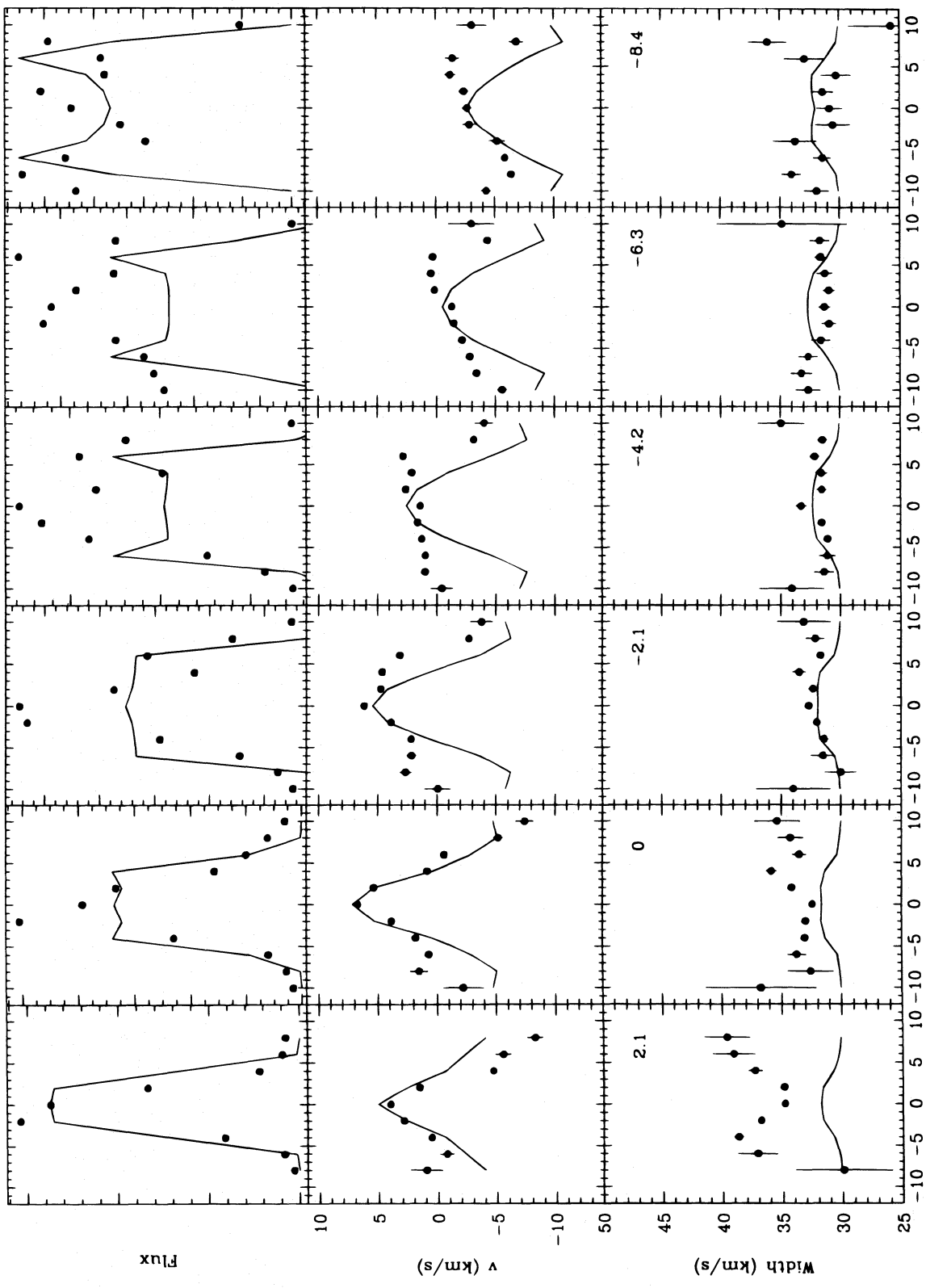

FIG. 9.—As for Fig. 8, but for the champagne model. Note the velocity centroid distribution is wider and in better agreement with the observations.

pagne model. To provide a component of motion parallel to the axis, we incorporated a component $v_{\rm champagne}$ given by

$$v_{\rm champagne} = \left(\frac{z' - l_{\rm max}}{z'_{\rm max} - l_{\rm max}}\right) v_{\rm champagne}({\rm max}) \qquad (8)$$

in the direction $z' = -\infty$. This component obviously accelerates linearly from the standoff distance to the tail, in reasonable agreement with the results of the detailed models for similar smoothly varying density gradients (Franco, Tenorio-Tagle, & Bodenheimer 1990). At the head of the cometary structure, the motion still appears to be dominated by the expansion of the ionization front perpendicular to the shell in many of the champagne models. This can be seen in the velocity field of the two-dimensional hydrodynamical calculations (see, e.g., Fig. 2 of Bodenheimer et al. 1979), for example. Of course, this is a similar velocity pattern to that in the bow shock model. Therefore, in our champagne models we also retain a component of the form of equation (4), albeit with a lower v_* that mimics the expansion speed of the ionization front. These two velocity components are added together to produce a total velocity field that contains the basic points of a champagne model.

The results for a champagne model that has all the other parameters the same as our bow shock model, except that $v_* = 10$ km s^{-1} and $v_{\rm champagne}({\rm max}) = 20$ km s^{-1}, are shown in Figures 8 and 9. We have also increased the offset velocity by 10 km s^{-1} to 92 km s^{-1}. This now represents the $v_{\rm LSR}$ of the exciting star and the ambient molecular cloud since they are not in significant relative motion in the champagne scenario. Hence, the offset velocity now agrees much better with the observed molecular cloud velocity. As expected, similar motions are seen at the head as in the bow shock model, but now we see a steep velocity gradient in the tail that is present in all the slit positions in Figure 8. Of course, we still cannot produce the decrease in velocity centroid ahead of the emission peak at the outermost slit positions. The champagne velocity field also produces increased line widths in the tail for the central slit positions, which is more at odds with the data than the bow shock model. By contrast, the same increase in line width toward the edge of the nebula in the tail means that those points are a better fit to the data than the bow shock model. Just as for the bow shock model, it is possible that turbulence could have a major impact on the line widths in this region in the champagne model (for example, gas streaming past clumped gas would give rise to turbulence). In Figure 9 the champagne model has slowed the falloff of the velocity centroid toward the edges but still not enough to match the data.

It is worth considering how well the champagne flow model we have just described compares with the hydrodynamical models in the literature. For example, Yorke et al. (1983) present radio continuum maps for champagne models of rather older H II regions. These models produce a somewhat more "filled-in" appearance than the observed limb-brightened structure seen in G29.96−0.02 and most other cometary H II regions. The velocity structure of these models is presented in Yorke et al. (1984) (see, e.g., their Fig. 1). The velocity centroid peaks just behind the intensity peak along the symmetry axis and retains a steep gradient toward the tail at large off-axis distances just as in our approximate champagne model. The behavior of our model ahead of the star is, of course, dominated by the residual bow shock component we have added in. In the original champagne flow model, the velocity field is largely static in this region. However, combining a champagne model with elements of a model in which the gasdynamics near the star is driven largely by a stellar wind (see, e.g., Turner & Matthews 1984) or by radiation pressure on dust (see, e.g., Yorke & Krügel 1977) may appear somewhat similar to our combined bow shock and champagne flow model. More detailed calculations of these mixed models are required to fully answer these questions, however.

5. CONCLUSIONS

We have demonstrated the value of our infrared techniques in studying the kinematical structures of young, heavily extinguished H II regions. The data we present here for G29.96−0.02 clearly show features not present in previous radio data that allow us to test the validity of the two proposed models in much greater detail. In particular we have shown that the regions in which the bow shock model has the poorest fit to the data are not at all well represented in the radio recombination line data of Wood & Churchwell (1991). Therefore, their conclusions, and those of Van Buren & Mac Low (1992) and Afflerbach et al. (1994), that G29.96−0.02 is completely consistent with a bow shock interpretation must be questioned.

From our own data, and the analytic approximation to the bow shock model we have employed, we find that the greatest discrepancies lie near the "head" of the region, and along the "sides." For the "head" of the region, we find the broadest lines are *ahead* of the point at which the line intensity reaches a maximum, whereas the bow shock model predicts they should coincide. This may be due to turbulent mixing processes in the interface between the ionized and molecular gas. Therefore, we do not consider it a strong argument against the bow shock model. Similar arguments could also be applied to the existence of this gas in the champagne flow model we have described.

The one aspect of the data that the bow shock model cannot explain away through an appeal to turbulence is the velocity gradient seen along the outer edge of the H II region in the "tail." Our velocity centroid data show large deviations from the model. Another way to demonstrate this is to compare the maps of line flux and velocity centroid. The bow shock model predicts that the observed velocities along the outer edge of the comet should be constant since we are seeing gas that is essentially comoving with the molecular cloud material, e.g., the lowest contour in the velocity centroid map in Figure 6 of Van Buren & Mac Low (1992) follows the outer edge of the emission measure. It can be seen that the opening angle of the velocity centroid is wider than that of the flux as was also apparent in the radio data (Fig. 5 of Van Buren & Mac Low 1992). In the champagne flow model (see, e.g., Bodenheimer et al. 1979), the velocity gradient behind the star is easy to explain; however, other means are required to produce the velocity gradient ahead of the star at the edge of the H II region. For both models presented here, it is this aspect of the data that presents the greatest challenge.

In summary, the motions in the tail of G29.96−0.02 are highly suggestive of a champagne flow, although our very simple model is still far from a good fit to all the data. Our results are consistent with the radio continuum maps of Fey et al. (1995) who also argue in favor of a champagne flow model on the basis of the combined radio and near-infrared morphology of the region. As advocated by Gaume et al.

(1994) and others, there is an urgent need to investigate champagne flows that include the effects of stellar winds since we know the latter exist in these regions, as well as taking more realistic density distributions into account. This will lead to a better understanding of how young massive stars affect their natal environments and further star formation.

S. L. L. would like to thank the Australian Nuclear Science and Technology Organisation for providing funding for the trip to UKIRT. We would also like to thank Tom Geballe and Tim Carroll for their help in obtaining these observations, and PATT for the allocation of telescope time on UKIRT. Last, we would like to thank the anonymous referee for suggestions that helped in the presentation of our data.

REFERENCES

Afflerbach, A., Churchwell, E., Hofner, P., & Kurtz, S. 1994, ApJ, 437, 697
Bashkin, S., & Stoner, J. O. 1975, Atomic Energy Levels and Grotrian Diagrams (Amsterdam: North-Holland)
Bodenheimer, P., Tenorio-Tagle, G., & Yorke, H. W. 1979, ApJ, 233, 85
Cesaroni, R., Churchwell, E., Hofner, P., Walmsley, C. M., & Kurtz, S. 1994, A&A, 288, 903
Cesaroni, R., Walmsley, C. M., Kömpe, C., & Churchwell, E. 1991, A&A, 252, 278
Churchwell, E., Walmsley, C. M., & Cesaroni, R. 1990, A&AS, 83, 199
Doherty, R. M., Puxley, P. J., Doyon, R., & Brand, P. W. J. L. 1994, MNRAS, 266, 497
Dyson, J. E. 1975, Ap&SS, 35, 299
Elmegreen, B. G., & Lada, C. 1977, ApJ, 214, 725
Fey, A. L., Gaume, R. A., Claussen, M. J., & Vrba, F. J. 1995, ApJ, 453, 308
Fich, M. 1993, ApJS, 86, 475
Franco, J., Shore, S. N., & Tenorio-Tagle, G. 1994, ApJ, 436, 795
Franco, J., Tenorio-Tagle, G., & Bodenheimer, P. 1989, Rev. Mexicana Astron. Astrofis., 18, 65
———. 1990, ApJ, 349, 126
Garay, G., Lizano, S., & Gomez, Y. 1994, ApJ, 429, 268
Garay, G., Rodríguez, L. F., & van Gorkom, J. H. 1986, ApJ, 309, 553
Gaume, R. A., & Claussen, M. J. 1990, ApJ, 351, 538
Gaume, R. A., Fey, A. L., & Claussen, M. J. 1994, ApJ, 432, 648
Herter, T., et al. 1981, ApJ, 250, 186
Hummer, D. G., & Storey, P. J. 1987, MNRAS, 224, 801
Humphreys, C. J. 1973, J. Phys. Chem. Ref. Data, 2, 519
Icke, V., Gatley, I., & Israel, F. P. 1980, ApJ, 236, 808
Israel, F. P. 1978, A&A, 90, 769
Koornneef, J. 1983, A&A, 128, 84
Kurtz, S., Churchwell, E., & Wood, D. O. S. 1994, ApJS, 91, 659
Landini, M., Natta, A., Salinari, P., & Moorwood, A. F. M. 1984, A&A, 134, 284
Lumsden, S. L., & Puxley, P. J., 1995, MNRAS, submitted
Mac Low, M.-M., Van Buren, D., Wood, D. O. S., & Churchwell, E. 1991, ApJ, 369, 395
Mountain, C. M., Robertson, D. J., Lee, T. J., & Wade, R. 1990, Proc. SPIE, 1235, 25
Oliva, E., & Origlia, L. 1992, A&A, 254, 466
Tenorio-Tagle, G. 1979, A&A, 71, 59
Tenorio-Tagle, G., Yorke, H. W., & Bodenheimer, P. 1979, A&A, 80, 100
Turner, B. E., & Matthews, H. E. 1984, ApJ, 277, 164
Van Buren, D., & Mac Low, M.-M. 1992, ApJ, 394, 534
Wood, D. O. S., & Churchwell, E. 1989, ApJS, 69, 831
———. 1991, ApJ, 372, 199
Yorke, H. W., & Krügel, E. 1977, A&A, 54, 183
Yorke, H. W., Tenorio-Tagle, G., & Bodenheimer, P. 1983, A&A, 127, 313
———. 1984, A&A, 138, 325